J. Vis. Commun. Image R. 22 (2011) 653–663

Contents lists available at SciVerse ScienceDirect

J. Vis. Commun. Image R.

journal homepage: www.elsevier.com/locate/jvci

High-quality non-blind image deconvolution with adaptive regularization

Jong-Ho Lee *, Yo-Sung Ho

Gwangju Institute of Science and Technology (GIST), 1 Oryong-dong, Buk-gu, Gwangju 500-712, Republic of Korea

ARTICLE INFO

Article history:
Received 14 December 2010
Accepted 15 July 2011
Available online 23 July 2011

Keywords:
Image deblurring
Non-blind image deconvolution
Ringing artifacts
Noise amplification
Local characteristics
Adaptive regularization
Fast deconvolution
Boundary artifacts reduction

ABSTRACT

Non-blind image deconvolution is a process that obtains a sharp latent image from a blurred image when a point spread function (PSF) is known. However, ringing and noise amplification are inevitable artifacts in image deconvolution since perfect PSF estimation is impossible. The conventional regularization to reduce these artifacts cannot preserve image details in the deconvolved image when PSF estimation error is large, so strong regularization is needed. We propose a non-blind image deconvolution method which preserves image details, while suppressing ringing and noise artifacts by controlling regularization strength according to local characteristics of the image. In addition, the proposed method is performed fast with fast Fourier transforms so that it can be a practical solution to image deblurring problems. From experimental results, we have verified that the proposed method restored the sharp latent image with significantly reduced artifacts and it was performed fast compared to other non-blind image deconvolution methods.

1. Introduction

One of the most common and unpleasant defects in photography is motion blur caused by camera shake. Especially, if a picture is taken in the dim light conditions, it takes long time to get enough light and the camera shake by hands results in a degraded image. If a motion blur is shift-invariant, recovering a true latent image from the degraded image reduces to image deconvolution. The blurring process is commonly modeled as a convolution of the true latent image and a point spread function (PSF) with additive noise:

$$B = K \otimes I + N, \tag{1}$$

where B is the degraded image, I is the true latent image, K is the PSF, and N is additive noise. Image deconvolution is a process to restore I from B.

If both the PSF and the latent image are unknown, the problem is called blind deconvolution. In blind deconvolution, the problem is challenging since both PSF and the latent image should be estimated from the blurred image. Thus, to facilitate the problem, early approaches assume simple parametric models for the PSF such as linear motion blur or out-of focus blur [1,2]. Additional input was also used in some methods. Ben-Ezra and Nayar attached a low-resolution video camera to a high-resolution still camera to help in recording the PSF [3]. Yuan et al. used a pair of images, a blurred image and a noisy image which was taken with fast shutter speed, to estimate the PSF and the latent image [4]. Recently, the PSF was estimated from a single image. Fergus et al. used a variational Bayesian method with natural image statistics to estimate the PSF [5]. Jia used an alpha matte that describes transparency changes caused by a motion blur for PSF estimation [6]. Shan et al. proposed the blind deconvolution method using a maximum a posteriori (MAP) to estimate both the PSF and the latent image from a single image [7]. However, it is very difficult to estimate the exact PSF from a single image. For example, the saturated pixels or homogeneous region on the blurred image prevent the PSF from being estimated correctly.

On the other hand, if the PSF is assumed to be known or estimated in other ways, the problem is reduced to estimate the latent image alone. This is called non-blind image deconvolution. Wiener filtering [8] and Richardson–Lucy method [9] are traditional and popular non-blind image deconvolution methods. Although these methods were proposed several decades ago, they are still widely used for image restoration because they are simple, fast, and give good results in case of the relative small blur. However, non-blind deconvolution is still an ill-posed problem although the PSF is known, so it gives rise to artifacts in the deconvolved image. The main artifacts are ringing and noise amplification. Fig. 1 shows the deconvolution result. Ringing is the ripple-like artifact that appears around strong edges in the deconvolved image as shown in Fig. 1(c). The PSF is often band-limited, so its frequency response shows zero or near-zero values at the high frequency. Therefore, the direct inverse of the PSF with the blurred image causes large signal amplification at the high frequency components and this is represented as the ringing near the edges and amplified noise. Especially, PSF estimation errors accelerate the ringing artifacts

* Corresponding author.
E-mail addresses: purmod@imrc.kist.re.kr (J.-H. Lee), hoyo@gist.ac.kr (Y.-S. Ho).

1047-3203/$ - see front matter © 2011 Elsevier Inc. All rights reserved.
doi:10.1016/j.jvcir.2011.07.010

Fig. 1. Ringing artifacts in image deconvolution. (a) Blurred image and estimated PSF. (b) Deconvolution result. (c) Magnified patch.

and give very unpleasant deconvolved results [7]. Various regularization techniques to reduce these artifacts are proposed. Chambolle and Lions proposed total variation regularization with Laplacian prior [10]. Levein et al. used a sparse prior with heavy-tailed distribution that shows quite good results with significantly reduced artifacts [11]. Shan et al. also exploit the image prior defined on their own to reduce artifacts in the deconvolved image [7]. Recently, Cho et al. proposed a content-aware image prior which adapt prior to the image contents. This prior is more effective to recover the latent image than other fixed image priors since the gradient profile of the image is changed according to textures [23]. All of them introduce image prior into the deconvolution, so they solve the MAP problem instead of maximum likelihood (ML) estimation. However, all these regularization methods using the MAP are effective only when the PSF size is small and the estimated PSF has no error. If the PSF size is large and the estimated PSF is incorrect, then the deconvolved image contains severe ringing or amplified noise. The strong regularization to reduce these severe artifacts destroys the image details in the deconvolved image, and this is inevitable problem in image deblurring since perfect PSF estimation is impossible.

We propose a non-blind image deconvolution method with adaptive regularization that controls the regularization strength adaptively according to the local characteristics. It reduces ringing and noise in a smooth region effectively and preserves image details in a textured region simultaneously. For adaptive regularization, we make reference maps that give right edge information so that textured region and smooth region can be distinguished well. Regularization strength is controlled adaptively referring to these reference maps. There are other several methods exploiting pilot images like reference maps in our algorithm to improve quality of deconvolution. Lou et al. use the deconvolved image with Tikhonov regularization as their pilot image for computing weights of non-local operator [24]. Takeda et al. also estimate the pilot image by Wiener filtering followed by kernel regression to compute weight matrix [25]. Dabov et al. use the regularized inversion using BM3D filter to estimate the pilot image [26]. All these pilot images are the estimates of the deconvolution results, so they give important information for deconvolution, and enable better deconvolution results to be achieved. However, since all pilot images in these methods are estimated using very simple method for computational advantage, they suffer from ringing artifacts when the estimated PSF is not correct and these artifacts in pilot images have bad influence on the final results. In our algorithm, the reference maps are elaborated using both blurred image and deconvolved image by adaptive regularization with hyper-Laplacian image prior. Thus, they give well-defined edge and texture information. Furthermore, proposed image deconvolution with adaptive regularization is performed very fast in the frequency domain using the fast Fourier transforms (FFTs). The experimental results show that the latent image with high-quality is recovered very fast from the blurred image compared to other various non-blind image deconvolution methods.

The rest of this paper is organized as follows. In the next Section, we will briefly review the conventional regularization techniques and present its limitations on recovering the high-quality latent image. In Section 3, we will introduce the high-quality non-blind image deconvolution with adaptive regularization. In Section 4, performance of the proposed method will be verified and the paper will be completed with conclusions in Section 5.

2. Conventional regularization methods

The most basic form of regularization is the Tikhonov regularization [12]. It is given as follows:

$$I^* = \arg\min_I \sum_{i=1}^{N}((I \otimes K - B)_i^2 + \eta |I_i|^2), \tag{2}$$

where i is the pixel index, and η is the regularization weighting factor that controls strength of regularization. Tikhonov regularization reduces artifacts quite well, but since it assumes the image to be smooth and continuous, it produces smooth results and fails to recover the sharper edges.

More advanced regularization techniques are proposed using the image prior. According to Bayes' theorem, the posteriori for the latent image is written as:

$$p(I|B) \propto p(B|I)p(I), \tag{3}$$

where $p(B|I)$ denotes the likelihood of the blurred image given the latent image, and $p(I)$ represents the image prior. The MAP solution of I can be obtained by minimizing the following energy:

$$I^* = \arg\min_I E(I), \tag{4}$$

where

$$E(I) = -\log p(I|B) = -\log p(B|I) - \log p(I). \tag{5}$$

The likelihood is based on noise, $N = B - I \otimes K$, and it can be assumed to follow Gaussian distribution [11] or Poisson distribution [13]. If the noise model is Gaussian and the image prior is assumed that the first derivative of image follows Laplacian distribution, Eq. (5) can be represented as:

$$E(I) = \sum_{i=1}^{N}((I \otimes K - B)_i^2 + \eta(|(I \otimes f_1)_i| + |(I \otimes f_2)_i|)), \tag{6}$$

where $f_1 = [1\ -1]$, $f_2 = [1\ -1]^T$, and η is the regularization weighting factor. This regularization technique is called total variation, and it takes into consideration the information that the image data set is blocky and discontinuous [10]. This method helps to obtain the discontinuities or steep gradients in the restored image.

Recently, various studies on global images have shown that the image gradients have heavier tails than a Gaussian or Laplacian distribution. Roth and Black modeled image statistics with a product of potentials defined on filter outputs [14]. Weiss and Freeman

Fig. 2. Deconvolution results with conventional regularization. (a) Blurred image and estimated PSF (b) Strong regularization result. (c) Weak regularization result.

used Gaussian Scale Mixture Fields of Experts (GSM FOE) model for image prior [15]. A simpler form of the heavy-tailed distribution of image gradients is the hyper-Laplacian model. Hyper-Laplacian image priors have been often used in image deblurring [11,16]. The hyper-Laplacian image prior can be modeled as:

$$p(I) \propto e^{-k|\nabla I|^{\alpha}} \quad \text{with} \quad 0.5 \leqslant \alpha \leqslant 0.8. \tag{7}$$

With the Gaussian noise model and the hyper-Laplacian image prior, Eq. (5) can be represented by

$$E(I) = \sum_{i=1}^{N}((I \otimes K - B)_i^2 + \eta(|(I \otimes f_1)_i|^{\alpha} + |(I \otimes f_2)_i|^{\alpha})), \tag{8}$$

where η is the regularization weighting factor.

On the other hand, Yuan et al. also proposed a regularization technique using a bilateral filter [17]. Although this regularization technique shows excellent results with preserved edges and reduced artifacts, it takes too much time to obtain a final result due to repetitive intra- and inter-scaling and filtering operation in each scale.

In all above conventional regularization techniques, the regularization weighting factor, η is applied to all pixels with the same intensity. Fig. 2 represents the deconvolution results with conventional regularization. The left one shows the deconvolution result with strong regularization and the right one is that of weak regularization. Levin's method was used for image deconvolution, and the regularization weighting factors of 0.1×10^{-1} and 0.1×10^{-9} were used for strong regularization and weak regularization respectively. Strong regularization in the image deconvolution helps to reduce the artifacts in the smooth region, but it blurs the edges in the textured region. Weak regularization preserves image details well, but it does not remove artifacts effectively. Therefore, the conventional regularization has limitations if the PSF estimation error is large or image noise is too severe to be ignored. Large PSF estimation error and severe noise give rise to severe ringing and noise amplification and those severe artifacts require strong regularization which destroys image details.

Furthermore, Eq. (8) is not a convex function, so it is difficult to get a solution optimizing Eq. (8). Commonly used method is an iteratively reweighted least squares (IRLS) method that solves a series of weighted least-squares problems with conjugate gradient (CG) [11]. In this method, since typically hundreds of CG iterations, each involving an expensive convolution of the current image estimate and the PSF, are needed, it takes too much time to process.

3. High-quality non-blind image deconvolution with adaptive regularization

The main idea of our algorithm is to change strength of regularization based on the reference map which indicates the smoothed region and textured region. In the smooth region, strong regularization is performed to suppress the artifacts and in the textured region, weak regularization is applied to preserve image details. The first reference map is estimated from the blurred image and the first adaptive regularization is performed based on the first reference map. Since the blurred image does not show right edge information, the first adaptive regularization does not work well. Thus, the second reference map is estimated using the first deconvolved image, and the second adaptive regularization is executed with the second reference map. All adaptive regularizations are performed in the frequency domain for fast computation. However this computation in the frequency domain causes boundary artifacts at the deconvolved image boundaries and these artifacts need to be removed. In this Section, we will cover each step of our algorithm in detail. Reference map estimation, adaptive regularization, fast computation of adaptive regularization, and how to reduce the boundary artifacts will be described thoroughly. The overall algorithm for high-quality non-blind image deconvolution with adaptive regularization is outlined in Algorithm 1.

Algorithm 1. High-quality non-blind image deconvolution with adaptive regularization

Require: Blurred image B, PSF K
Require: Expansion width T, smoothness window radius r
Require: Threshold for 1st reference image estimation T_a
Require: Threshold for 2nd reference image estimation T_b
Require: Regularization weighting factor for smooth region $\eta 1$
Require: Regularization weighting factor for textured region $\eta 2$
B_ex = `img_exp`(B, T, r) *%Expand blurred image for RBA*
Y = `rgb2ycbcr`(B)
Y = Y(:, :, 1) *%Extract luma from blurred image*
for $i = 1$ to 2
  if $(i = 1)$ **then**
    Ref1 = `issmoothl`(Y, T_a) *%Estimate 1st reference map*
    I1 = `deconv_adapregu`(B_ex, K, $\eta 1$, $\eta 2$, Ref1) *%1st adaptive regularization*
  else
    Ref2 = `issmooth2`(B, I1, T_b) *%Estimate 2nd reference map*
    I2 = `deconv_adapregu`(B_ex, K, $\eta 1$, $\eta 2$, Ref2) *%2nd adaptive regularization*
  end if
end for
I = I2(1:`size`(B, 1), 1:`size`(B, 2), :)
output: I

3.1. Reference map estimation

The reference map is for classifying the smooth region and the textured region correctly. The estimated reference map is used for adaptive regularization. It is difficult to obtain right edge information from the blurred image directly, so the reference map is estimated twice.

The first reference map is estimated from the blurred image. Since the smooth region which has no edges in the blurred image is still the smooth region in the recovered image, the smooth region, Ω, is defined as follows:

$$p \in \Omega \text{ if } Eg(p) < T_a \text{ and}$$

$$Eg(p) = \left(\sum_{h \in W_x} h + \sum_{h \in W_y} v \right) \Big/ N_{total}, \tag{9}$$

where $Eg(p)$ is the edge strength at the pixel location p on the blurred image, $W_x = W \otimes [1\ -1]$, $W_y = W \otimes [1\ -1]^T$, W is the 3×3 window whose center is located on p, and N_{total} is the total number of pixels in W. $T_a = 0.3 \times 10^{-2}$ is used for the experiment. The textured region is the region outside Ω. The first estimated reference map with Eq. (9) is represented in Fig. 3. The white pixels mean the smooth region and dark pixels the textured region.

The first adaptive regularization is performed with the estimated first reference map. We will explain adaptive regularization in detail in Section 3.2. The second reference map is estimated from the deconvolved image with the first adaptive regularization. The deconvolved image with the first adaptive regularization shows much better edge information than the blurred image, so better reference map can be estimated from it. Shan et al. also define a locally smooth region in their algorithm which functions similarly to our reference map [7]. They constrain the blurred image gradient to be similar to the unblurred image gradient in the smooth region. However, since they define the locally smooth region based on only blurred image where edge information is not correct, their anti-ringing effect is not good near the edges.

At the second reference map estimation, we use other criterion to distinguish the textured region from the smooth region elaborately instead of Eq. (9). Fig. 4 represents step signals in the blurred image and the deconvolved image. The derivative of step signal in the deconvolved image is larger than that in the blurred image. Thus, the derivative of p on the blurred image, $\nabla B(p)$, and the derivative of p on the deconvolved image, $\nabla I(p)$, are compared, and if the difference, $\nabla I - \nabla B$, is larger than the predefined threshold, T_b, the pixel p is defined to be in the textured region. Otherwise, the pixel is defined to be in the smooth region. We used 0.025 as a T_b value for the experiments. The deconvolved image with the first adaptive regularization and the estimated second reference map are represented in Fig. 5. In the second reference map, the white pixels mean the smooth region and the dark pixels the textured region as the first reference map. The second reference map distinguishes the textured region from the smooth region much better than the first reference map.

3.2. Adaptive regularization

Adaptive regularization is performed based on the estimated reference map. We use the MAP solution as a basic frame for image deconvolution. For convenience, MAP solution is represented again in Eq. (10).

$$I^* = \arg\min_I \sum_{i=1}^{N} ((I \otimes K - B)_i^2 + \eta(|(I \otimes f_1)_i|^\alpha + |(I \otimes f_2)_i|^\alpha)). \tag{10}$$

In the conventional regularization, the same value of η is applied to all pixels, but the proposed method controls η value adaptively according to the local characteristics. In the textured region, small η value is applied, and in the smooth region, large η value is applied. Furthermore, we use the model of the spatially random distribution of image noise as an image noise model, $N = I \otimes K - B$ [7]. This model states that not only image noise but also its higher-order partial derivatives follow Gaussian distributions with different standard deviations. This model is helpful to restore finer details in the deconvolved image than the normal distribution model. Based on these, we modify Eq. (10) as follows:

$$I^* = \arg\min_I \sum_{i=1}^{N} \left(\sum_{\partial^* \in \Theta} \tau_{k(\partial^*)} (\partial^* I \otimes K - \partial^* B)_i^2 + \eta_p (|(I \otimes f_1)_i|^\alpha + |(I \otimes f_2)_i|^\alpha) \right), \tag{11}$$

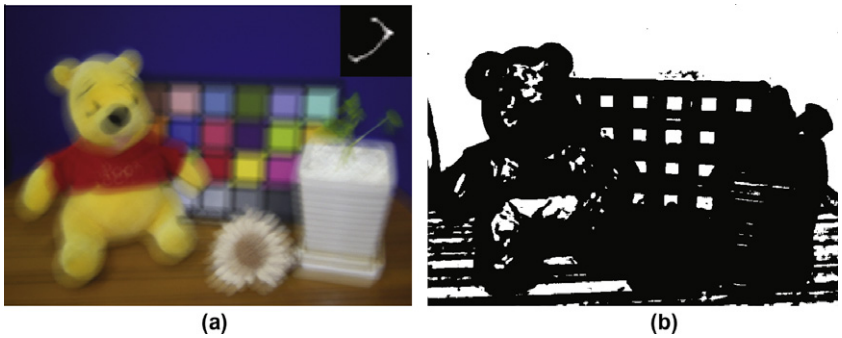

Fig. 3. First reference map estimation. (a) Blurred image. (b) First reference map.

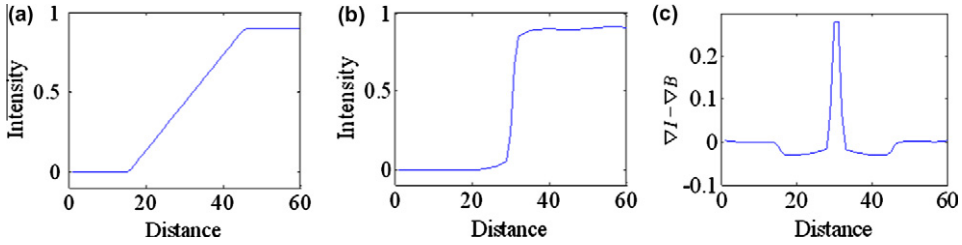

Fig. 4. Step signal characteristics of blurred image and deconvolved image. (a) Step signal in blurred image. (b) Step signal in deconvolved image. (c) $\nabla I - \nabla B$.

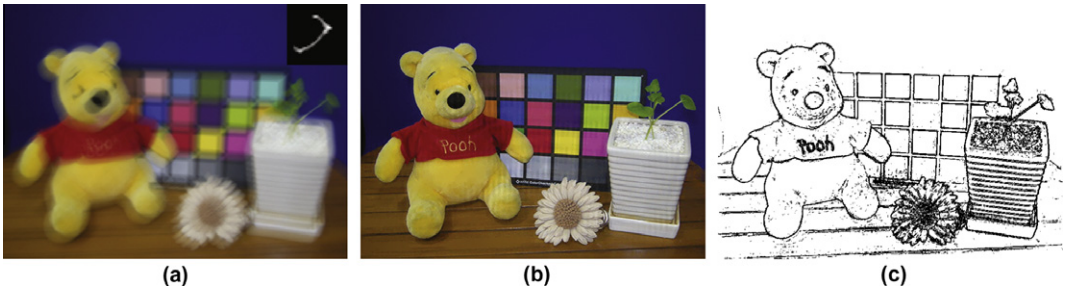

Fig. 5. Second reference map estimation. (a) Blurred image. (b) Deconvolved image with first adaptive regularization. (c) Second reference map.

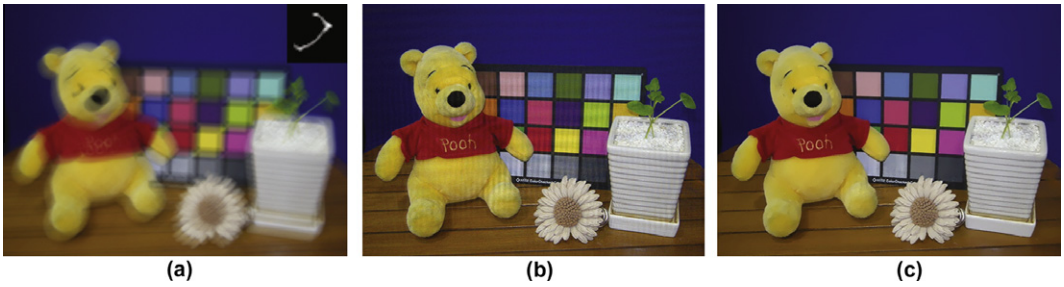

Fig. 6. Effect of adaptive regularization. (a) Blurred image. (b) Deconvolution result without adaptive regularization. (c) Deconvolution result with adaptive regularization.

where ∂^* denotes the operator of any partial derivative with $k(\partial^*) = q$ representing its order. $\partial^* N = \partial^*(I \otimes K - B)$ follows a Gaussian distributions with standard deviation $\sigma_q = \sigma_0$, where σ_0 denotes the standard deviation of N. $\Theta = \{\partial_0, \partial_x, \partial_y, \partial_{xx}, \partial_{xy}, \partial_{yy}\}$ represents a set of partial derivative operators [7]. The η_p is equal to 0.5×10^{-2} if the pixel p is located on the smooth region and 2.5×10^{-4} in the textured region. The effect of adaptive regularization in the image deconvolution is represented in Fig. 6. The middle image is deconvolved result by Eq. (11) with the same η_p equal to 2.5×10^{-4} for all pixels. The right image is deconvolved result with different η_p values according to the local characteristics as defined above. The artifacts noticeable in the deconvolved result with the conventional regularization are removed significantly in the deconvolved result with the adaptive regularization while preserving image details.

3.3. Fast adaptive regularization

Adaptive regularization can be performed fast in the frequency domain with the alternating minimization. The alternating minimization was originally proposed by Geman et al. [18,19] and this technique was used for image deconvolution in various algorithms [7,20,21]. We simply modified Krishnan's fast algorithm using hyper-Laplacian image prior for our adaptive regularizaiton [20]. If we substitute $I \otimes f_1$ and $I \otimes f_2$ with ω_1 and ω_2 respectively, Eq. (11) can be modified as follows:

$$I^* = \arg\min_{I,\omega} \sum_{i=1}^{N} \left(\sum_{\partial^* \in \Theta} \tau_{k(\partial^*)} (\partial^* I \otimes K - \partial^* B)_i^2 + \frac{\beta}{2} ((I \otimes f_1 - \omega_1)_i^2 + (I \otimes f_2 - \omega_2)_i^2) + \frac{\lambda_p}{2} (|(\omega_1)_i|^{2/3} + |(\omega_2)_i|^{2/3}) \right). \quad (12)$$

For convenient calculation, η_p is replaced with $\lambda_p/2$, and this does not affect the performance of the algorithm. $(I \otimes f_j - \omega_j)^2$ term is for constraint of $I \otimes f_j = \omega_j$ and we use 2/3 for α. β is a weight that is varied during the optimization. As β becomes large, the solution of Eq. (12) is converges to that of Eq. (11). The β is varied from 0.1×10^{-2} to 256 by integer powers of $\sqrt{2}$, and for each β, $\omega = [\omega_1, \omega_2]$ and I are calculated alternatively. First, the initial I is set to B, and ω is calculated. If fixed I is given, Eq. (12) is reduced to the problem of solving for ω.

$$\omega^* = \arg\min_{\omega} \left(\frac{\lambda_p}{2} |\omega|^{2/3} + \frac{\beta}{2} (\omega - v)^2 \right), \quad (13)$$

where $v = I \otimes f_j$. ω^* satisfying the above equation is the solution of the following quartic equation.

$$\omega^4 - 3v\omega^3 + 3v^2\omega^2 - v^3\omega + \frac{\lambda_p^3}{27\beta^3} = 0. \quad (14)$$

The ω satisfying Eq. (14) can be obtained by Ferrari's method. Since the derivatives v of the image normalized to 1 are usually placed from -0.6 to 0.6, ω values are tabulated for the specific λ_p, β and 10,000 different values of v within the range of -0.6 and 0.6. Thus, ω are obtained very fast using the table for the input images.

Given a fixed value of ω from the previous iteration, Eq. (12) is quadratic in I. The optimal I is:

$$\left(\sum_{\partial^* \in \Theta} 2\tau_{k(\partial^*)} A_{\partial^*}^T A_{\partial^*} A_k^T A_k + \beta \left(A_{f_1}^T A_{f_1} + A_{f_2}^T A_{f_2} \right) \right) \mathbf{i} = \sum_{\partial^* \in \Theta} 2\tau_{k(\partial^*)} A_{\partial^*}^T A_{\partial^*} A_k^T \mathbf{b} + \beta \left(A_{f_1}^T \omega_1 + A_{f_2}^T \omega_2 \right), \quad (15)$$

where A_{∂^*}, A_k, A_{f_1}, and A_{f_2} are the matrix forms of ∂^*, K, f_1, and f_2 respectively, and $\mathbf{i}$ and $\mathbf{b}$ are vector forms of I and B such that the product of the matrix and vector is equal to the convolution of the originals. Applying 2D FFTs, we can obtain I directly as follows:

$$I^* = F^{-1} \left\{ \frac{Numer}{Denom} \right\}, \quad (16)$$

where

$$Numer = \sum_{\partial^* \in \Theta} \tau_{k(\partial^*)} \overline{F\{\partial^*\}} \circ F\{\partial^*\} \circ \overline{F\{K\}} \circ F\{B\} + \frac{\beta}{2} (\overline{F\{f_1\}} \circ F\{\omega_1\} + \overline{F\{f_2\}} \circ F\{\omega_2\}) \quad (17)$$

and

$$Denom = \sum_{\partial^* \in \Theta} \tau_{k(\partial^*)} \overline{F\{\partial^*\}} \circ F\{\partial^*\} \circ \overline{F\{K\}} \circ F\{K\} + \frac{\beta}{2}(\overline{F\{f_1\}} \circ F\{f_1\} + \overline{F\{f_2\}} \circ F\{f_2\}). \quad (18)$$

Here, $F\{\cdot\}$ and $F^{-1}\{\cdot\}$ represent Fourier and inverse Fourier transform respectively, $\overline{\{\cdot\}}$means complex conjugate, and $\circ$ means element-wise multiplication.

3.4. Reducing boundary artifacts

In the blurring process, the blurred pixels are generated with not only the image inside the Field of View (FOV) of the observation but also part outside the FOV. The part outside the FOV cannot be used in the deconvolution and this missing information causes ringing artifacts around the image boundary when the image is deconvolved using the FFT. Discrete Fourier Transform (DFT) assumes the periodicity of the data, so the missing information will be taken from opposite side of the image when performing FFT. However, since this data taken from the opposite side is not the same as the original data, the boundary artifacts are occurred.

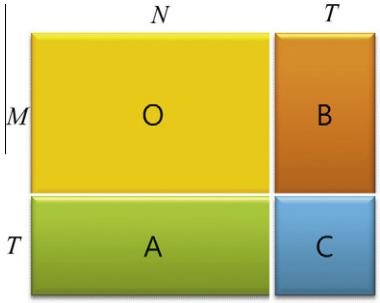

Fig. 7. Expansion of the blurred image for reducing boundary artifacts O: blurred image A, B, C: padding blocks.

The main idea to reduce the boundary artifacts is as follows. We expand the original blurred image such that the intensity and gradient are maintained at the border between the original image and the expanded part. The basic concept to solve the problem is similar to Liu and Jia's algorithm [22], but our algorithm is faster and requires lower memory achieving comparable quality since the number of padding blocks is smaller. Fig. 7 represents the expanded image for reducing boundary artifacts. O is the original blurred image, and A, B, and C are the three padding blocks. Each padding block is constructed such that the periodicity of the image is guaranteed and pixels in the padding block have smooth intensities not to cause ringing artifacts. We first start with the construction for the padding block A.

Let $X(i,:)$ and $X(:,j)$ denote the ith row and jth column in a image block X. The size of the original image is $M \times N$ and the size of the padding block A is $T \times N$, where T is the expansion width. The first row and the last row of the block A is filled first with the last row and the first row of the original blurred image respectively.

$$A(1,:) = O(M,:), \quad (19)$$

$$A(T,:) = O(1,:). \quad (20)$$

Next, the most outer two rows of the unpadded rectangular begin to be padded alternatively. The upper line is padded according to:

$$A(i,j) = \frac{\sum_{k=-r}^{r}(w_{1k}A(i-1,j+k)+w_{2k}A(T-i+2,j+k))}{\sum_{k=-r}^{r}(w_{1k}+w_{2k})}, \quad (21)$$

where w_{1k} and w_{2k} are distances from (i,j) to $(T-i+2,j+k)$ and from (i,j) to $(i-1,j+k)$ respectively, and $k \in \{-r,\ldots,r\}$, and r is a window radius that controls the smoothness in the horizontal direction. The lower line is padded according to:

$$A(T-i+1,j) = \frac{\sum_{k=-r}^{r}(w_{3k}A(i,j+k)+w_{4k}A(T-i+2,j+k))}{\sum_{k=-r}^{r}(w_{3k}+w_{4k})}, \quad (22)$$

where w_{3k} and w_{4k} are distances from $(T-i+1,j)$ to $(T-i+2,j+k)$ and from $(T-i+1,j)$ to $(i,j+k)$ respectively. This procedure is repeated for $i = 2$ to $T/2$. The block B is constructed with the similar

Fig. 8. Reducing boundary artifacts. (a) Blurred image and estimated PSF. (b) Deconvolution result without RBA algorithm. (c) Deconvolution result with RBA algorithm.

Fig. 9. Comparison of reducing boundary artifacts algorithm. (a) Liu et al.'s. (b) Ours.

manner to the block A. The only difference is the padded direction. The pixels in the block B are padded column by column.

The block C is computed after the block A and the block B are constructed. First, the most outer pixels of the block C are padded according to:

$$C(:,1) = A(:,N), \tag{23}$$
$$C(:,T) = A(:,1), \tag{24}$$
$$C(1,:) = B(M,:), \tag{25}$$
$$C(T,:) = B(1,:). \tag{26}$$

Next, the inner pixels are padded:

$$C(i,j) = \frac{\sum_{k=-r}^{r}(w_{1k}C_{1k} + w_{2k}C_{2k} + w_{3k}C_{3k} + w_{4k}C_{4k})}{\sum_{k=-r}^{r}(w_{1k} + w_{2k} + w_{3k} + w_{4k})}, \tag{27}$$

where C_{1k}, C_{2k}, C_{3k}, and C_{4k} are reference pixel values from the upper, bottom, left, and right directions respectively. The weighting factors w_{1k}, w_{2k}, w_{3k}, and w_{4k} are defined according to the distance from the current pixel location to the reference pixel location from each direction. This procedure is repeated until all the other pixels inside the block C are padded.

This expanded blurred image is used for image deconvolution instead of the original blurred image. After image deconvolution, the result image is cropped to the original size.

Fig. 8 shows the effect of our reducing boundary artifacts (RBA) algorithm. The middle and the right images are the results of our method with the same parameter setting, but the middle one used the general blurred image and the right one used the expanded blurred image formed according to the RBA algorithm followed by cropping to the original size after deconvolution. The boundary artifacts in the deconvolved image without RBA algorithm are reduced significantly with the RBA algorithm.

Fig. 9 shows the comparison of result from our RBA algorithm and Liu et al.'s. Shan et al.'s algorithm was used for image deconvolution [7]. Even though we use smaller number of padding blocks with smaller size than Liu et al.'s method, our result shows comparable performance.

4. Experimental results and analysis

We applied our algorithm to the synthesized image and the real blurred image. The synthesized image was generated by

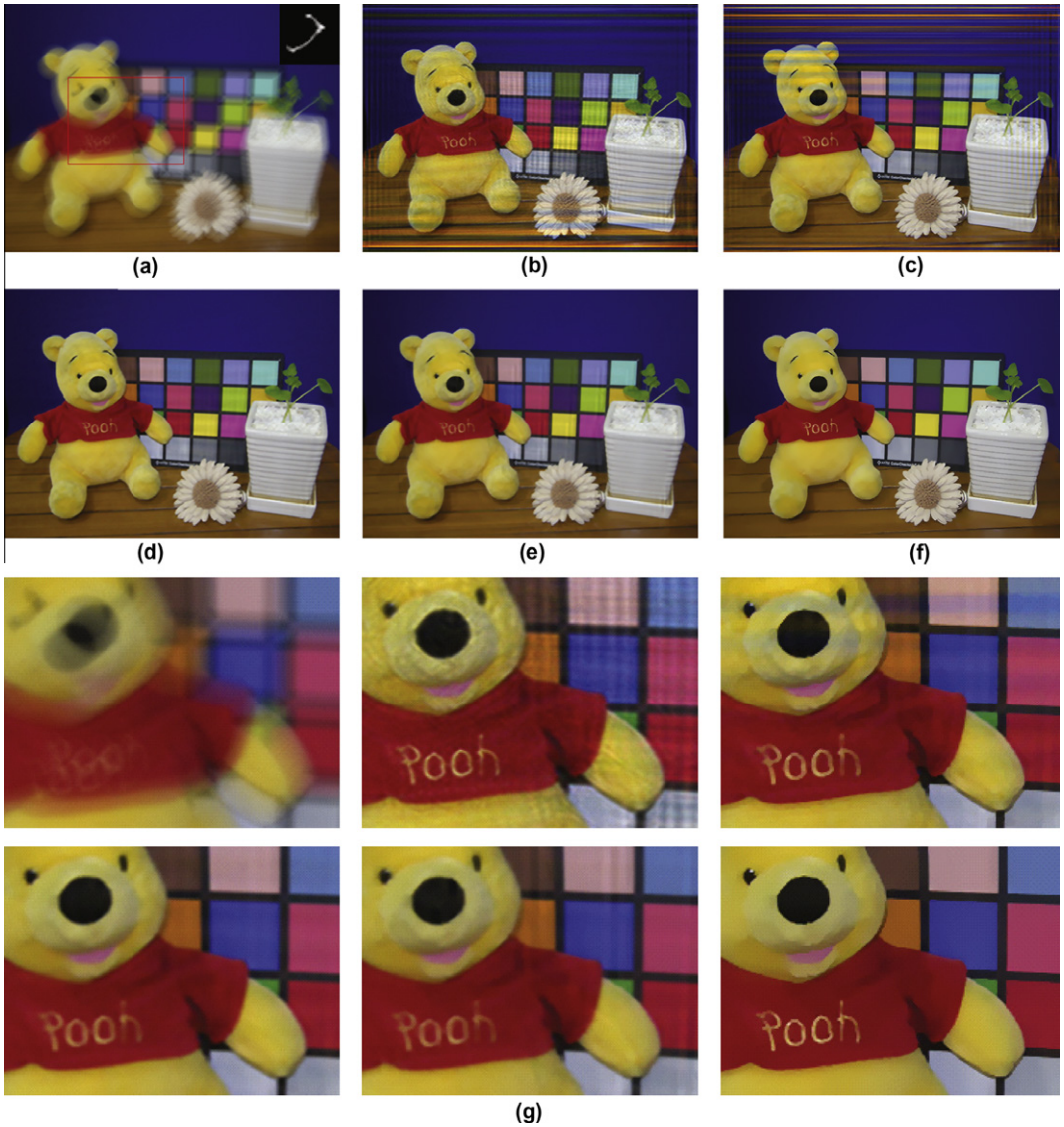

Fig. 10. Pooh. (a) Blurred image and estimated PSF. (b) Richardson–Lucy method. (c) TV regularization. (d) Levin's. (e) Shan's. (f) Proposed. (g) Close-up views of (a)–(f).

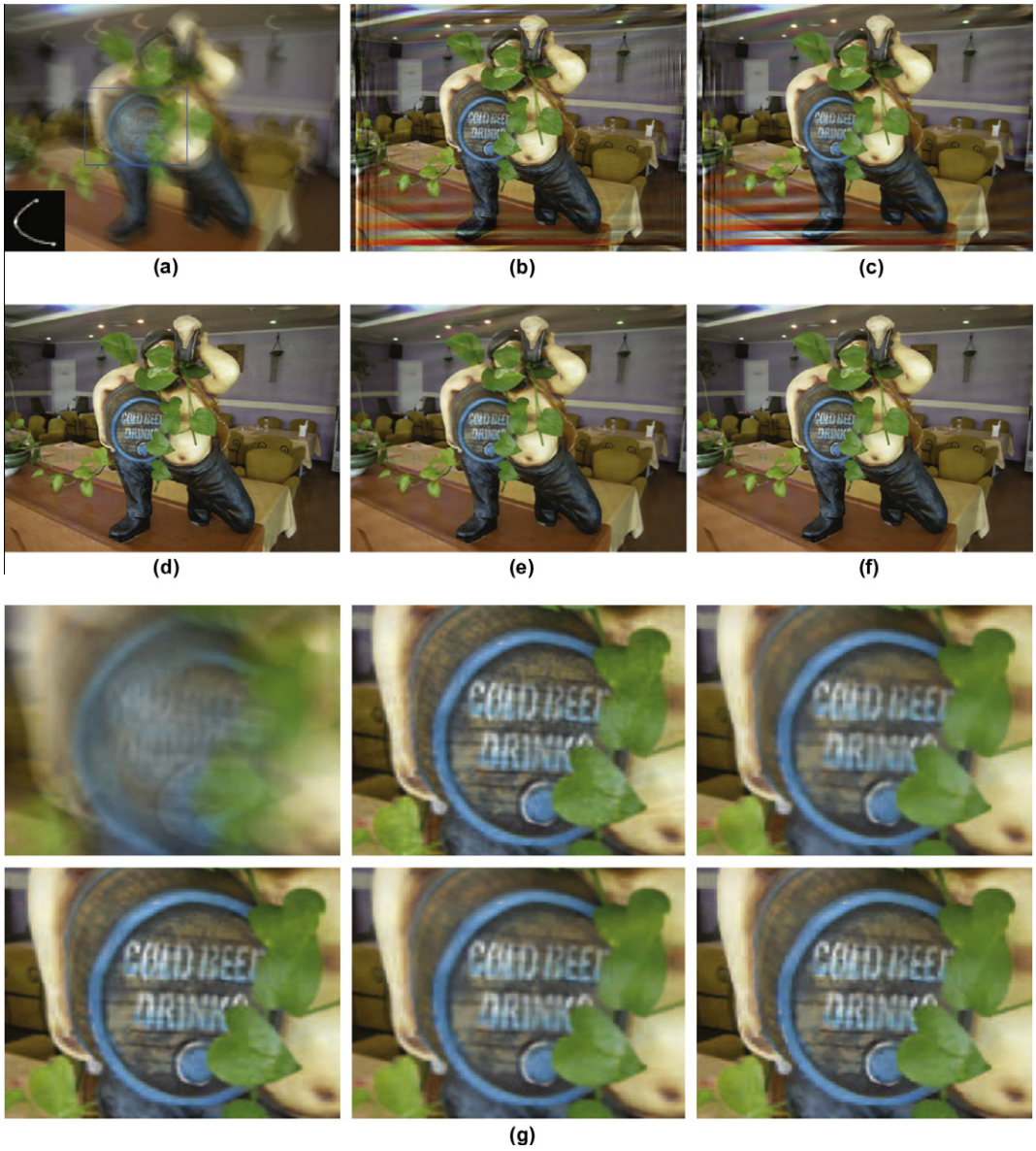

Fig. 11. Beer. (a) Blurred image and estimated PSF. (b) Richardson–Lucy method. (c) TV regularization. (d) Levin's. (e) Shan's. (f) Proposed. (g) Close-up views of (a)–(f).

convolving the artificial PSF and the original sharp image. For the synthesized image, both objective quality and subjective quality were checked. For the real blurred image, only subjective quality was measured. For testing the performance of our algorithm, we compared the results of our algorithm to those of four other non-blind image deconvolution methods, the standard Richardson–Lucy (RL) method [9], Total variation (TV) regularization [10], Levin's method [11] and Shan's non-blind deconvolution method [7]. They are popular non-blind image deconvolution methods due to their outstanding performances. For fare comparison, we tuned the regularization parameters of all algorithms to produce the best results.

Fig. 10 shows the comparison of the subjective quality for the synthesized Pooh image. The PSF is estimated by Shan's non-blind image deconvolution algorithm [7]. The estimated PSF size is 37×37, and the size of blurred image is 664×489. The RL method preserves edges well but produces the severe ringing and noise since it does not exploit regularization. Besides, it is performed in the frequency domain, so it gives rise to severe boundary artifacts in the deconvolved image. The TV regularization reduces ringing

Table 1
Comparison of SNRs for the Pooh image.

Method	SNR_R (dB)	SNR_G (dB)	SNR_B (dB)	SNR_Y(dB)
RL	8.92	12.25	6.68	11.48
TV	6.14	9.86	4.04	9.55
Levin's	20.76	20.05	17.95	19.75
Shan's	19.82	19.36	17.47	18.88
Proposed	21.10	20.54	18.31	20.49

Table 2
Comparison of SNRs for the Beer image.

Method	SNR_R (dB)	SNR_G (dB)	SNR_B (dB)	SNR_Y(dB)
RL	8.65	6.41	5.82	7.76
TV	7.98	5.44	3.92	6.75
Levin's	15.63	15.49	15.11	15.59
Shan's	14.74	15.20	14.95	14.96
Proposed	16.06	15.79	15.38	16.09

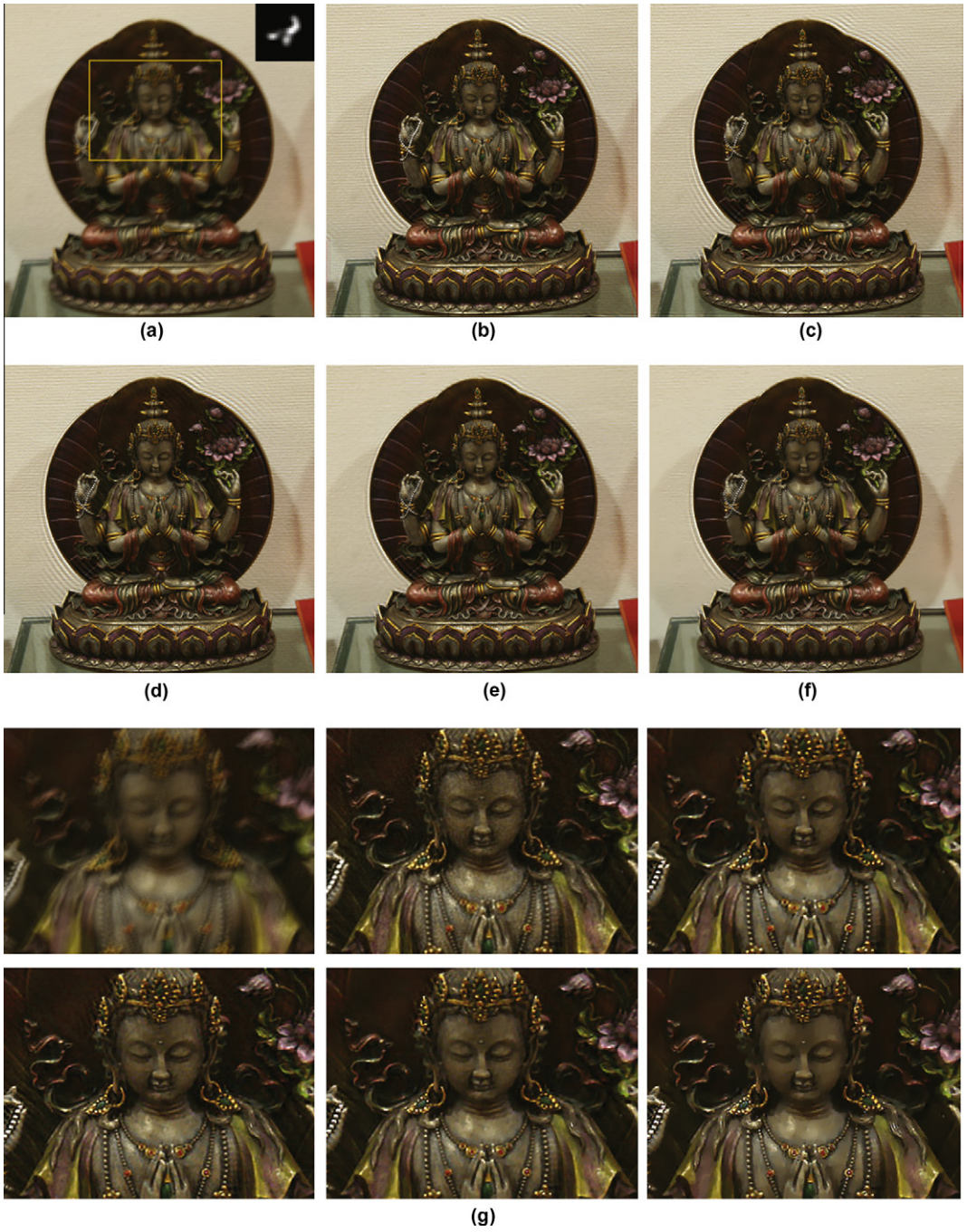

Fig. 12. Statue. (a) Blurred image and estimated PSF. (b) Richardson–Lucy method. (c) TV regularization. (d) Levin's. (e) Shan's. (f) Proposed. (g) Close-up views of (a)–(f).

and noise significantly, but image details are also reduced. The reduced details are the effect of using the Laplacian image prior instead of the hyper-Laplacian image prior. The TV regularization also generates the boundary artifacts due to FFT calculation. The Levin's algorithm and the Shan's algorithm reduce ringing and noise effectively without large image details loss due to advanced image priors, but they show limitations in case of large PSF errors since the regularization weighting factors with the same intensities are applied to all pixels of the image. However, our algorithm shows the excellent result with reduced ringing and noise in smooth region, while preserving image edges well by adjusting the regularization weighting factor according to the local characteristics.

Table 3
Comparison of complexities.

	RL (secs)	TV (secs)	Levin's (secs)	Proposed (secs)
Pooh	91.26	75.03	329.88	66.91
Beer	91.16	55.02	329.52	66.99
Statue	208.86	187.98	1110.54	121.94

Fig. 11 shows other results for the synthesized Beer image. The characters in the image are clear and the artifacts such as ringing and noise in the background are reduced significantly with our algorithm.

For the synthesized images, the objective quality is also measured. Tables 1 and 2 show the comparison of objective quality

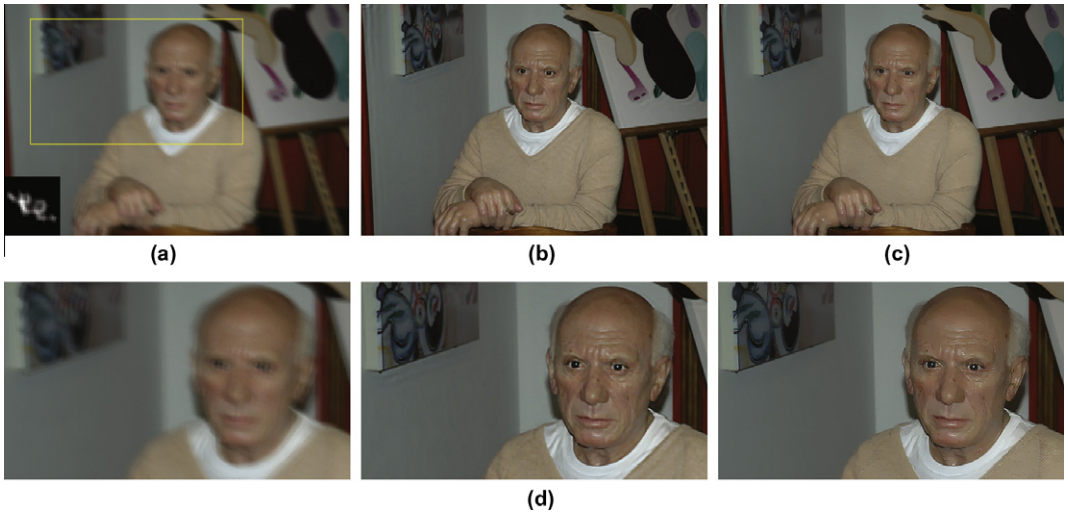

Fig. 13. Picasso. (a) Blurred image and estimated PSF. (b) Shan's. (c) Proposed. (d) Close-up views of (a)–(c).

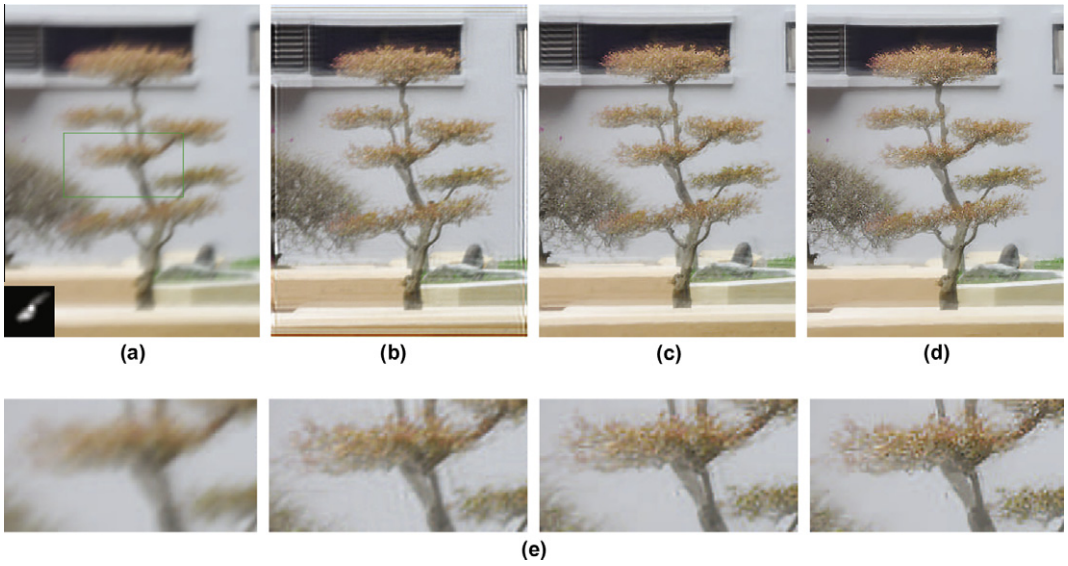

Fig. 14. Red tree. (a) Blurred image and estimated PSF. (b) Richardson–Lucy method. (c) Shan's. (d) Proposed. (e) Close-up views of (a)–(d). (For interpretation of the references in colour in this figure legend, the reader is referred to the web version of this article.)

for Pooh and Beer images respectively. We used Eq. (28) for the comparison metric. We calculated and compared the SNR for R, G, B channels and luminance component of the deconvolved images. Our algorithm shows the best performance when compared to other non-blind image deconvolution methods.

$$SNR(dB) = 10\log_{10}\left(\frac{\|I-\mu(I)\|^2}{\|I-I^*\|^2}\right), \tag{28}$$

where I is the original image, $\mu(I)$ is the mean of I, and I^* is the deconvolved image.

Next, we made an experiment with the real blurred image. We tested the performance with the image used in [7], and the test image was obtained from author's website.[1] The size of the blurred image is 903×910, and the size of the PSF is 25×25. The PSF is estimated by the Fergus' algorithm [5]. The results of our algorithm and other non-blind image deconvolution methods are represented in Fig. 12. The proposed method preserves fine image details, while suppressing artifacts.

Furthermore, we compared the complexity of our algorithm to other non-blind image deconvolution methods. All source codes are programmed with the MATLAB, and they are tested in AMD Athlon II X2 250 processor 3.23 GHz with 2.0 GB RAM. Since the image prior used in the proposed method is hyper-Laplacian, the energy function is non-convex and is not easy to optimize. However, with the alternating minimization and FFTs, the proposed algorithm shows faster speed than not only IRLS used in Levin's method which is the commonly-used optimization method to solve the non-convex problem but also other popular non-blind image deconvolution methods. The operation times for the proposed method and other non-blind image deconvolution methods are compared in Table 3.

Figs. 13 and 14 show other results of the images from [7]. In Fig. 13, ringing artifacts are not observed in the wall and fine details of the face are clear in our result when they are compared to the Shan's result. In Fig. 14, it can be verified that our method

[1] http://www.cse.cuhk.edu.hk/~leojia/projects/motion_deblurring/index.html.

shows superior edge-preserving ability compared to other non-blind image deconvolution methods.

5. Conclusion

In this paper, we propose a high-quality non-blind image deconvolution method with adaptive regularization. The most notorious artifacts at image deconvolution are ringing and noise amplification. These artifacts can be reduced by regularization using the image prior that represents global statistics of the image, but strong regularization for reducing severe artifacts at image deconvolution does not preserve image details well. In the image deconvolution, we controlled regularization strength referring to the reference map indicating the textured region and the smooth region to preserve image details, while suppressing artifacts. In addition, the proposed method is practical considering complexity by fast FFT operations. The experimental results show that our approach restores the high-quality latent image from the blurred image very fast compared to other non-blind image deconvolution methods.

Acknowledgments

This research was supported by the MKE (The Ministry of Knowledge Economy), Korea, under the ITRC (Information Technology Research Center) support program supervised by the NIPA (National IT Industry Promotion Agency) (NIPA-2010-(C1090-1011-0003)).

References

[1] Y. Yitzhaky, I. Mor, A. Lantzman, N.S. Kopeika, Direct method for restoration of motion-blurred images, Journal of the Optical Society of America A: Optics, Image Science, and Vision 15 (1998) 1512–1519.
[2] S.K. Kim, J.K. Paik, Out-of-focus blur estimation and restoration for digital auto-focusing system, Electronics Letters 34 (1998) 1217–1219.
[3] M.R. Ben-Ezra, S.K. Nayar, Motion deblurring using hybrid imaging, Proc. IEEE Conference on Computer Vision and Pattern Recognition 1 (2003) 657–664.
[4] L. Yuan, J. Sun, L. Quan, H.Y. Shum, Image deblurring with blurred/noisy image pairs, ACM Transactions on Graphics 26 (2007) 1–10.
[5] R. Fergus, B. Singh, A. Hertzmann, S.T. Roweis, W.T. Freeman, Removing camera shake from a single photograph, ACM Transactions on Graphics 25 (2006) 787–794.
[6] J. Jia, Single Image motion deblurring using transparency, Proceedings of IEEE Conference on Computer Vision and Pattern Recognition (2007) 1–8.
[7] Q. Shan, J. Jia, A. Agarwala, High-quality motion deblurring from a single Image, ACM Transactions on Graphics 27 (2008).
[8] N. Wiener, Extrapolation, Interpolation, and Smoothing of Stationary Time Series, MIT Press, 1964.
[9] L. Lucy, An iterative technique for the rectification of observed distributions, Astronomical Journal 79 (1974) 745–754.
[10] A. Chambolle, P.L. Lions, Image recovery via total variation minimization and related problems, Numerische Mathematik 76 (1997) 167–188.
[11] A. Levin, R. Fergus, F. Durand, W.T. Freeman, Image and depth from a conventional camera with a coded aperture, ACM Transactions on Graphics 26 (2007) 70–77.
[12] A. Tikhonov, On the stability of inverse problems, Doklady Akademii Nauk SSSR 39 (5) (1943) 195–198.
[13] N. Dey, L. Blanc-Fraud, C. Zimmer, Z. Kam, P. Roux, J. Olivo-Marin, J. Zerubia, Richardson–Lucy algorithm with total variation regularization for 3D confocal microscope deconvolution, Microscopy Research Technique 69 (2006) 260–266.
[14] S. Roth, M.J. Black, Fields of experts: a framework for learning image priors, in: Proceedings of IEEE Conference on Computer Vision and Pattern Recognition, 2005.
[15] Y. Weiss, W.T. Freeman, What makes a good model of natural images?, Proceedings of IEEE Conference on Computer Vision and Pattern Recognition (2007) 1–8
[16] N. Joshi, L. Zitnick, R. Szeliski, D. Kriegman, Image deblurring and denoising using color priors, Proceedings of IEEE Conference on Computer Vision and Pattern Recognition (2009) 1550–1557.
[17] L. Yuan, J. Sun, L. Quan, H.Y. Shum, Progressive inter-scale and intra-scale non-blind image deconvolution, ACM Transactions on Graphics 27 (2008).
[18] D. Geman, G. Reynolds, Constrained restoration and recovery of discontinuities, IEEE Transactions on Pattern Analysis and Machine Intelligence 14 (1992) 367–383.
[19] D. Geman, C. Yang, Nonlinear image recovery with half-quadratic regularization, IEEE Transactions on Pattern Analysis and Machine Intelligence 4 (1995) 932–946.
[20] Y. Wang, J. Yang, W. Yin, Y. Zhang, A new alternating minimization algorithm for total variation image reconstruction, SIAM Journal on Imaging Sciences 1 (2008) 248–272.
[21] D. Krishnan, R. Fergus, Fast image deconvolution using hyper-Laplacian priors, Proceedings of the Advances in Neural Information Processing Systems 22 (2009) 1–9.
[22] R. Liu, J. Jia, Reducing boundary artifacts in image deconvolution, IEEE International Conference on Image Processing (2008).
[23] T.S. Cho, N. Joshi, C.L. Zitnick, B.K. Sing, R. Szeliski, W.T. Freeman, A content-aware image prior, Proceedings of IEEE Conference on Computer Vision and Pattern Recognition (2010) 169–176.
[24] Y. Lou, X. Zhang, S. Osher, A. Bertozzi, Image recovery via nonlocal operators, Journal of Scientific Computing 42 (2010) 185–197.
[25] H. Takeda, S. Farsiu, P. Milanfar, Deblurring using regularized locally adaptive kernel regression, IEEE Transactions on Image Processing 17 (2008) 550–563.
[26] K. Dabov, A. Foi, K. Egiazarian, Image restoration by sparse 3D transform-domain collaborative filtering. in: Proceedings SPIE Electronic Imaging, 2008.